Autofluorescence Characteristics of Normal Foveas and Reconstruction of Foveal Autofluorescence from Limited Data Subsets

R. Theodore Smith, **Jan P. Koniarek**, **Jackie Chan**, **Takayuki Nagasaki**, **Janet R. Sparrow**, and **Kevin Langton**
Department of Ophthalmology, Columbia University, New York, New York.

Abstract

Purpose—To develop mathematical and geometric models of the nonuniform autofluorescence (AF) patterns of foveas of normal subjects and to reconstruct these models from limited subsets of data.

Methods—Confocal scanning laser ophthalmoscope (cSLO) AF fundus images of normal maculae were obtained from both eyes of 10 middle-aged subjects. They were filtered and contrast enhanced, to obtain elliptical isobars of equal gray levels (GLs) and determine the isobars' resolutions, eccentricities, and angles of orientation. The original image data were fit with a mathematical model of elliptic quadratic polynomials in two equal zones: the center and the remaining annulus.

Results—The AF images segmented into nested concentric GL isobars with GLs that increased radially from the least-fluorescent center. The mean isobar resolution was $31 \pm 7 \mu$m. The geometric eccentricity of the ellipses increased from 0.42 ± 0.12 centrally to 0.52 ± 0.14 peripherally ($P = 0.0005$), with mean axes of orientation peripherally $97.12 \pm 15.46°$. The model fits to the complete image data had mean absolute normalized errors ranging from $3.6\% \pm 3.7\%$ to $7.3\% \pm 7.1\%$. The model fits to small subsets (1% to 2% of total image data) had mean absolute errors ranging from $3.7\% \pm 3.8\%$ to $7.3\% \pm 7.2\%$.

Conclusions—Normal AF fundus images show finely resolved, concentric, elliptical foveal patterns consistent with the anatomic distribution of fluorescent lipofuscin, light-attenuating macular pigment (MP), cone photopigment, and retinal pigment epithelial (RPE) pigment in the fovea. A two-zone, elliptic, quadratic polynomial model can accurately model foveal data. This model may be useful for image analysis and for automated segmentation of pathology.

There is increasingly strong interest in noninvasive analysis of retinal disease, especially as related to age-related macular degeneration (AMD), the leading cause of vision impairment and blindness in the Western world.[1,2] One of the major methods of such analysis is through the use of the confocal laser scanning ophthalmoscope (cSLO), which in its autofluorescence (AF) mode can record the complex signal predominantly from autofluorescent lipofuscin granules in the RPE.[3-9] These fluoresce strongly in response to 488-nm laser light, and abnormalities of their distribution are leading indicators of the severity of AMD.[10-13]

Corresponding author: R. Theodore Smith, Columbia University, 635 W 165 Street, Suite 314, New York, NY 10032; rts1@columbia.edu..

However, these images are not determined by the AF of lipofuscin alone, a fact that complicates their interpretation. One complicating factor is the absorption of the 488-nm light by the macular pigment (MP), especially the carotenoids lutein and zeaxanthin.[14,15] This absorption is greatest in the center of the macula, which on fundus photographs and under visual observation is characterized by strong yellow color.[16] There is similar absorption of the 488-nm light by melanin granules in the RPE,[17] which also have greater density centrally. Finally, photopigments, particularly cone photopigments in the fovea, will attenuate the signal if they are not completely bleached.

AF images obtained with the SLO from normal retinas display characteristic nonuniform, elliptical patterns centered on the macula. These patterns are darker in the center, indicating lower fluorescence (hypofluorescence) resulting from greater light absorption by the attenuating pigments, and are lighter (hyperfluorescent) peripherally. Depending on their appearance, they have been classified by one group of investigators,[18] as belonging to four subtypes (phenotypes) based on relative size and intensities of the hypo- and hyperfluorescent regions. To complicate the matter further, the overall patterns are not permanent, but change with age. AF increases in older individuals, with increased lipofuscin at the posterior pole, at least to age 70,[19,20] whereas the measured ratio of foveal AF to maximum AF intensity has been reported not to vary with age.[3] Quantification of these patterns has so far been lacking and is needed to make progress in assessment of retinal disease.

At present, in the clinical setting, lesions of AMD are manually graded on fundus photographs by trained graders who use semiquantitative scales.[21-26] Clinical evaluations of increased AF and decreased AF lesions are likewise qualitative in character.[27] Manual grading has several drawbacks, such as poor repeatability and extensive and time-consuming training necessary for adequate proficiency. Because of these drawbacks, there has been a great deal of interest in developing automated digital techniques for quantification of macular disease.[28-33] Accurate mathematical models of normal images could form the basis for such techniques.

As an initial step in this direction, the two-dimensional structure of normal foveal AF images was examined in two distinctly different but related ways. In the first, a pattern of gray-level (GL) isobars in the actual image data was determined by applying standard image-processing techniques of filtering and contrast enhancement. The resultant patterns, which were found to be approximately concentric and elliptical, were then analyzed to determine geometric properties of eccentricity, axis of orientation, and resolution. This was followed by the second step, the development of a mathematical model that could accurately represent the image data. Because the first analysis showed approximate elliptical contours in the data, the model chosen was based on quadratic polynomial functions, which mathematically generate precise elliptical contours in two dimensions. The mathematical model was then tested for accuracy of fit to real image data as well as data reconstruction from small data subsets.

Methods

Subjects and Image Acquisition

We examined both eyes of 10 normal white and Hispanic middle-aged subjects 32 to 64 years of age (seven women aged 32, 36, 50, 53, 56, 62, and 64 years, and three men aged 36, 56 and 59 years). All subjects had normal results in dilated retina examinations. Slit lamp examinations were performed to ensure that no lens opacities were present that would result in abnormal absorption of laser light by the crystalline lens. Informed consent was obtained from all subjects, and the study was performed with institutional review board approval and according to the tenets of the Declaration of Helsinki. After pupillary dilation, fundus AF images were recorded with a cSLO (model HRA/HRA2; Heidelberg Engineering, Dossenheim, Germany). This instrument uses blue laser light at 488 nm for illumination and a barrier filter at 500 nm

to limit the captured light to autofluorescent structures. The radiant power through the pupil is 180 μW, giving a retinal irradiance of 227 μW/cm^2 for a 30° square field. The time for acquisition was approximately 15 to 30 seconds, as would be normal in the clinical setting. As will be discussed, cone photopigment bleaching was incomplete after this exposure.

The AF images consisted of bit-mapped laser scans, 512×512 pixels in size, centered on the macula. The gain setting was the same for each scan. Each image was the average of three to six raw scans automatically composed by the SLO software. The scans were registered precisely and summed to increase the signal-to-noise ratio, and then a histogram stretch was applied to yield images that could be visualized directly (the "normalized" scan). These stretches were close to, but not strictly, linear transformations, and the stretch factor varied between images depending on the dynamic range of the raw scans.

Image Preprocessing

All images had a scale of approximately 15 μm per pixel. For processing and analysis the images were imported into image-analysis software (Photoshop 5.5; Adobe Systems Inc., San Jose, CA) as bit-mapped files consisting of 256 GLs for each pixel. Local image variation was evaluated by calculating the image standard deviations in small (240×240-μm) boxes. We found that, on this small scale, the images were all somewhat noisier than those reported by von Ruckmann et al.[5] After a Gaussian filter of 36-μm radius was applied to the entire image, the standard deviations in such boxes were no more than five GLs, similar to the images analyzed by von Ruckmann et al.[5] This filter had no noticeable effect on larger image features or isobar patterns, as defined later. The image was then cropped to a 100 pixels square (1500-μm^2) centered on the point of lowest foveal fluorescence, and the fovea was defined as the enclosed circle 1500 μm in diameter. All subsequent analyses were performed on these preprocessed foveal images. A typical image of the area of interest is shown in Figure 1.

Image Analysis

Line Scans—For the 20 eyes, GLs were recorded from horizontal and vertical line scans of 100-pixel length and 1-pixel width through the center of the fovea. These data were normalized by subtracting the lowest GL (foveal center) from each scan. The means of the 10 horizontal and vertical scan data of the right eyes were computed at each point to give mean right eye horizontal and vertical scans. Mean left eye horizontal and vertical scans were computed similarly. We also separately normalized the original line scan data by dividing by the lowest GL from each scan. A separate set of mean normalized right eye and left eye scans was likewise calculated. For each of these scans, the central minimum was unity and the peripheral maximum was the peak-to-trough (peripheral maximum/foveal minimum) ratio. Normalization by division largely removed the effect of the histogram stretch on the scan profile introduced by the HRA software, to the extent that it was linear.

Isobar Pattern Generation—Pattern generation is shown in Figure 2 in two typical normal patients. The preprocessed foveal images are shown on Figures 2A and 2D. The foveal data were then further filtered (Gaussian blur, 180-μm radius) to establish a regular shading pattern of GL isobars, each isobar having a single GL. This filter radius was determined empirically to provide the most useful patterns for analysis. In practice, the fovea then segmented into 20 to 30 GL isobars, each separated from its neighbor by 1 unit step and each becoming progressively more hyperfluorescent (lighter) from the center to the periphery. This pattern of isobars could now be studied without further digital manipulation. However, since unit steps of GL are imperceptible to the human eye, a contrast-enhancing histogram stretch (the "Auto Levels" feature in Photoshop) was applied to make the patterns clear to the human observer, as well as for illustration (Figs. 2B, 2E). Once contrast enhanced, the isobars were geometrically unchanged as sets, but neighboring isobars were separated by several units of GL. It is important

to note that, after this step, absolute GLs are not meaningful. Some characteristic individual isobars, still too fine to be discernible in these illustrations, are highlighted for emphasis in Figures 2C and 2F.

Our purpose was to find the best geometric description of the isobars from our data. In particular, we wanted to determine whether they followed the overall oval geometry of the clinically apparent luteal and RPE pigment distribution and the fluorescent lipofuscin. Hence, we postulated that theoretical isobar patterns are concentric ellipses with GLs increasing radially from the hypofluorescent center. We anticipated that the real patterns would be neither precisely elliptical nor strictly concentric, but very close to both, unless retinal vessels or focal abnormalities impinged on them.

Determination of Isobar Resolution and Eccentricities

The gradient of GLs in the foveal region is described quantitatively as the isobar resolution, a measure defined as the radius of the fovea, nominally $750\,\mu$m, divided by the number of isobars in the foveal pattern. This definition is the equivalent to the average width of an isobar, and hence is a measure of how finely the isobars divide the fovea.

For each image, two isobars were selected for eccentricity measurement. The first, or inner, was chosen to have approximately a 500-μm diameter (for example, the inner isobars in Figs. 2C, 2F). The second, or outer, was the largest complete isobar in the pattern. The major and minor axes, orientations, and eccentricities of the two isobars were calculated with the mathematical morphology software from an image-analysis toolkit (MatLab, ver. 5.5; the MathWorks, Natick, MA). This software calculates a best-fit bounding ellipse for any object, together with these associated geometric quantities for that ellipse, but does not provide a measure of goodness of fit. We therefore elected to illustrate the geometric quantities and goodness of fit in four characteristic examples (Fig. 3). It was immediately apparent that the inner isobars were all nearly circular and therefore lacked meaningful angular orientation. The angular orientations of the major axes of the outer isobars were recorded.

The Mathematical Model

We constructed models of foveal AF in two subregions: an inner region of $750\,\mu$m in diameter and the outer annulus of $1500\,\mu$m outer diameter. Two regions were chosen because, from the appearance of the AF patterns, it was obvious that a steeper gradient of AF existed in the inner region and a less steep gradient in the outer region. The data in each region were fit with a quadratic polynomial, and the transition between the regions was smoothed with a radial spline function. Average absolute errors and standard deviations were calculated as a percentage of the total gray-scale range of the preprocessed foveal data. These data had noise reduced by a small-scale filter, as described, but are not the large-scale filtered data used to generate the isobars. The complexity of the data is evident in Figure 4, which shows an example of fitting the model to a particular foveal image (Figs. 4A, 4B), using the model to reconstruct the image data from a uniform grid subset of this data (Figs. 4C, 4D), and using the model to reconstruct the image data from a nonuniform grid subset of the data (Figs. 4E, 4F).

Specifically, the preprocessed AF GLs were considered to be functions of their pixel coordinates (x, y) in the x–y plane. The general quadratic has the following form:

$$q(x,y) = ax^2 + bxy + cy^2 + dx + ey + \text{constant}. \tag{1}$$

For each image, a unique quadratic in two variables was fit by custom software (developed in Mathematica 5.0; Wolfram Research Inc., Champaign, IL), applying least-squares methods to

the AF data set in each subregion to optimize the six coefficients (*a*, *b*, *c*, *d*, *e*, constant). Thus, a quadratic, *q*1, was fit to the data in the inner region and a second quadratic, *q*2, to the data in the annulus (for a total of 12 coefficients). To create a smooth fit at the boundary of the two regions, we used a sigmoidal radial cubic spline function to interpolate the quadratics. An example of a foveal AF image and the associated contour graph of the smooth model fit to this foveal data are displayed in Figures 4A and 4B.

The accuracy of each model fit to the AF data was determined as follows: the absolute values of the errors at each (*x*, *y*) point in two dimensions were treated as a single data set *E*. We then calculated the mean and SD of *E* and scaled these results by dividing by the net GL range of the original data to give the mean error ± SD as a percentage of the data range.

To determine whether the model could reconstruct the foveal image data from a limited amount of data, such as from images containing pathology that obscures part of the background, a grid of evenly spaced pixel data was taken from the two regions (as in Fig. 4C). It comprised 1.1% of the pixels in the annulus and 1.7% of the pixels in the inner disc. The two-zone quadratic model was fit for each image to this grid of data. The resultant model, shown for a particular image in Figure 4D, was then compared to the complete AF data set and errors calculated as before.

We also selected a random subset of data points from the two regions (Fig. 4E). It comprised 1.1% of the pixels in the annulus and 2.1% of the pixels in the inner disc. The two-zone quadratic model was again fit for each image to this data subset. The resultant model, shown for a particular image in Figure 4F, was then compared with the complete AF data set and errors calculated as before.

Results

The GL isobars in AF scans of 20 normal retinas from 10 individuals formed a set of concentric, approximately elliptical annuli, with the GL of fluorescence increasing outward along any radius from the least-fluorescent central disc. The annular isobars were all complete (with occasional discontinuities limited to a few pixels) until the boundary of the foveal region was reached, when they became partial annuli and ultimately progressively hyperfluorescent arcs (see Fig. 2B). The isobars were more circular centrally and became more elliptical toward the periphery of the fovea, with the geometric eccentricity of the patterns increasing from 0.42 ± 0.12 centrally to 0.52 ± 0.14 peripherally (*P* = 0.0005). The axes of orientation of the outer ellipses clustered around 90°. The mean axis of orientation was 97 ± 15°, with 17 of 20 within 90 ± 30°. The average foveal isobar resolution was 31 ± 7 μm (range, 21– 47 μm). The isobar resolutions centrally were even finer, usually ~15 μm (1 pixel) in width. We did not find any major differences in the patterns themselves or their isobar resolutions when analyzed according to age, race, or sex in this small sample.

The AF range (difference between the maximum and the minimum GL) varied from 30 to 82 (mean, 74 ± 11). The minimum AF, by definition, was always at the foveal center. The arcs of highest fluorescence were always in the temporal quadrant. This finding was confirmed quantitatively by vertical and horizontal line scans of 10 left and 10 right eyes. When the line scans were normalized by subtracting the lowest GL, the mean GL temporally for left eyes was greater than nasally, inferiorly, or superiorly for all radii greater than 510 μm (at or above the 0.05 significance level, by two-tailed *t*-test). A similar finding of elevated mean GLs temporally held for right eyes, with radii greater than 585 μm. When the line scans were renormalized by dividing by the lowest GL, the results were almost identical. The mean GL ratio temporally in the left eyes was significantly higher than nasally with radii greater than 515 μm, and in right eyes, with radii greater than 600 μm. There were no significant differences between GL ratios

superiorly and inferiorly in the left or right eyes, or between left eyes temporally compared with right eyes. In our 20 eyes, the maximum GL ratios were always temporal and ranged from 1.2 to 2.6 (mean, 1.72 ± 0.37). The means of 10 horizontal and vertical line scans, normalized by division, through the foveas of left and right eyes are shown in Figure 5.

The patterns generated by the model fit to subsets of data are also strikingly similar to the normal foveal patterns (compare Figs. 2B and 4B). Despite the simplicity of the model compared with the complexity of the raw data, the mean absolute errors of the fits for each subject (as defined in the mathematical model in Methods) were only small percentages of the net gray-scale ranges. For example, in Figure 4, the mean absolute error of the model for this image was 3.4 GLs (normalized to 4.2% of the net image range of 80). The model fits to the complete image data for all subjects had mean absolute normalized errors ranging from those of the best-fit image, $3.6\% \pm 3.7\%$, to those of the worst-fit image, $7.3\% \pm 7.1\%$. The model fits to the grid subsets of image data had mean absolute errors ranging from $3.7\% \pm 3.8\%$ to $7.3\% \pm 7.2\%$, and from random data subsets the range was $3.2\% \pm 3.4\%$ to $9.1\% \pm 9.2\%$.

Discussion

We have demonstrated that the geometry of normal AF images in the fovea exhibits a set of concentric elliptical isobars of isofluorescence, with the GL of fluorescence increasing outward along any radius from the least-fluorescent, darker center. The elliptically shaped patterns in the image data tended to be more circular centrally and more vertically elongated peripherally. The highest GLs were always temporal, consistent with the findings of Delori et al.[19] A simple noise filter and contrast enhancement revealed geometry of convex GL isobars, with isobar resolutions averaging 30 μm in the periphery, but in the central foveal area closer to single-pixel resolution (15 μm).

A model of foveal AF data was constructed from a set of two quadratic polynomials. For each image, the coefficients (12 in all) of the quadratics were individually determined by least-squares methods, and accurate fits were obtained in all cases. The robustness of the model was attested by the fact that it could also be used to reconstruct foveal data from small grid subsets of data (or randomly chosen subsets of data) comprising less than 2% of the entire image, with average errors 3% to 7% of net image range (slightly more in the random case). In practice, in a pathologic situation one would generally have access to a much larger subset of normal background for reconstruction, and so these data represent an extreme test of the model. Further, the fact that such small fractions of image data yielded such similar and accurate model reconstructions suggests that the AF signal itself, when devoid of noise, has a similar underlying geometric simplicity which can be captured by knowing its values at a small number of points. Likewise, the extraordinary geometric regularity and precise isobar resolutions of the foveal AF patterns demonstrated in the current study suggest that the normal spatial variations of luteal, RPE, and cone pigment—the main absorbers of blue light in the fovea— and lipofuscin itself, the source of the AF signal, have similar circular to elliptic regularity and equally fine resolution.

These AF patterns are in fact consistent with the known anatomic distributions of these pigments. The MP is a mixture of the carotenoids lutein and zeaxanthin and has a well characterized optical density spectrum, with peak absorption at 457.8 nm.[14] The distribution of this pigment peaks centrally and tapers radially. Its anatomic density drops to half-maximum within a diameter of 500 to 600 μm, reaches a quarter-maximum at a diameter of approximately 1000 μm, and from there tapers slowly outward to a low constant level.[34] There is considerable variation in the central optical density (compared with an eccentric reference point) of MP, reported to range from 0.21 to 0.77 (median 0.53) density units in one group of seven normal subjects at the peak absorption.[14] Another group found an MP density of 0.0 to 0.64 (mean,

0.32 ± 0.24) in 34 normal control subjects aged 20 to 65 years.[35] Because the relative optical density of macular pigment at 488 nm is approximately 0.8, the corresponding central optical densities of the former subjects would range from 0.17 to 0.62 (median, 0.42) density units, and in the latter from 0.0 to 0.51 (mean, 0.25). If we estimate the densities at 750-μm radius to be a quarter of these values,[34] then the change in density from the center to 750 μm would range from 0.13 to 0.47 (median, 0.32) in the former group, and from 0.0 to 0.38 (mean, 0.19) in the latter. The corresponding AF images would thus have central minima deeper by factors ranging from 1.3 to 3.0 (median, 2.1) or from 1.0 to 2.4 (mean, ~1.5).

Photoreceptor photopigments are incompletely bleached after an approximate 15- to 30-second exposure to the HRA in AF mode (retinal irradiance, 227 μW/cm^2) and thus contribute to the patterns obtained in clinical image acquisition. The main contribution is from cones (37% bleached at 15 seconds, 56% at 30 seconds), rather than rods (density 0.3 at 12°, negligible centrally, 78% bleached after 15 seconds).[36] With a cone density of 0.8 density units centrally at the absorption peak of 550 nm, one can calculate (for cone absorption at 488 nm equal to 0.49 relative to 550 nm) that the optical density of cone photopigment to 488 nm centrally after 15 to 30 seconds is 0.25 to 0.17 density units. The cone density at the foveal periphery (approximately 2.5°), by two-way density measurements, is approximately 0.25,[37] and so the change in optical density from center to periphery is approximately 0.55 density units. After bleaching and correction for absorption at 488 nm, the difference in optical density between center and periphery would thus range from 0.17 (15 seconds) to 0.12 (30 seconds). These density differences would give deeper minima (ratio of peak to trough) in measured AF at the center relative to the periphery by factors of 1.5 and 1.3, respectively, and a greater gradient centrally than if bleaching were complete. For rods, the corresponding optical density maximum would be 0.06 density units at 12° to 15° from the fovea, negligible in the fovea itself. The cone bleaching in clinical settings is thus likely to be somewhat variable and necessarily incomplete, because, even after 90 seconds of exposure, the cone bleaching plateaus at 78%. This yields a deeper central minimum in AF by a factor of 1.15. If the cones are contributing a factor of 1.3 to 1.5 and if MP contributes factors between 1.0 and 2.4, as just calculated according to Davies and Morland,[35] one would expect the peripheral fovea to central AF peak-to-trough ratios on the HRA to vary between 1.3 and 3.6 in these subjects. In our 10 subjects, these ratios ranged from 1.2 to 2.6 (mean, 1.72 ± 0.37), a range that is quite consistent. The peak-to-trough ratios expected from the data of Bone et al.[14] would be somewhat higher (1.7– 4.5).

Lipofuscin has a minimum centrally and tends to increase to the foveal edge in both vertical and horizontal meridians.[19] This distribution pattern also contributes to central hypofluorescence. The melanin in RPE has a broad absorbance across the visible spectrum and also has highest density centrally.[38]

Other reflectors and absorbers that may affect the observed pattern include the retinal nerve fiber layer (RNFL) and the lens. The cutoff filter used to measure AF blocks the reflectance of the RNFL at 488 nm. Because the RNFL has no known AF, its contribution to the observed AF should be minimal. To eliminate suppression of AF by the lens, we used only eyes that were clear of cataract. Lens absorption, in any case, may be expected to reduce the range and resolution of the pattern but not its geometry. Intrinsic lens AF is eliminated by the confocal image acquisition. There was no significant difference in any of the parameters between the men and women or as function of age in this middle-aged population.

In summary, the precise foveal AF patterns we described appear to be some combination of cone photopigment and luteal pigment optical density maps superimposed on the intrinsic lipofuscin-derived AF signal. The mathematical model we developed herein accurately represented the original scan data in this complex circumstance. The model was also robust,

in that it could reconstruct the original scan data from very limited data subsets, hence could be useful for analysis of AF images from diseased maculas, much in the manner of what has been done for drusen by using fundus photographs.[39,40] For example, foveal hyperfluorescence,[20,27] embedded in the darker central pattern, could be delineated and quantified more accurately than is possible at present.

To our knowledge, this is the first detailed two-dimensional description of this geometry from AF images. A significant benefit of our analysis is that it is achieved with a commercially available cSLO and inexpensive commercial imaging software run on a desktop computer and lends itself to dissemination for standardized analysis of foveal images.

Acknowledgments

References

1. Friedman DS, O'Colmain BJ, Munoz B, et al. Prevalence of age-related macular degeneration in the United States. Arch Ophthalmol 2004;122:564–572. [PubMed: 15078675]

2. Klein R, Peto T, Bird AC, Vannewkirk MR. The epidemiology of age-related macular degeneration. Am J Ophthalmol 2004;137:486–495. [PubMed: 15013873]

3. von Ruckmann A, Fitzke FW, Bird AC. Distribution of fundus autofluorescence with a scanning laser ophthalmoscope [comment]. Br J Ophthalmol 1995;79:407–412. [PubMed: 7612549]

4. von Ruckmann A, Fitzke FW, Bird AC. In vivo fundus autofluorescence in macular dystrophies. Arch Ophthalmol 1997;115:609–615. [PubMed: 9152128]

5. von Ruckmann A, Fitzke FW, Bird AC. Fundus autofluorescence in age-related macular disease imaged with a laser scanning ophthalmoscope. Invest Ophthalmol Vis Sci 1997;38:478–486. [PubMed: 9040481]

6. von Ruckmann A, Fitzke FW, Bird AC. Distribution of pigment epithelium autofluorescence in retinal disease state recorded in vivo and its change over time. Graefes Arch Clin Exp Ophthalmol 1999;237:1–9. [PubMed: 9951634]

7. Holz FG, Bellman C, Staudt S, Schutt F, Volcker HE. Fundus autofluorescence and development of geographic atrophy in age-related macular degeneration. Invest Ophthalmol Vis Sci 2001;42:1051–1056. [PubMed: 11274085]

8. Delori FC, Goger DG, Dorey CK. Age-related accumulation and spatial distribution of lipofuscin in RPE of normal subjects. Invest Ophthalmol Vis Sci 2001;42:1855–1866. [PubMed: 11431454]

9. Delori FC, Dorey CK, Staurenghi G, Arend O, Goger DG, Weiter JJ. In vivo fluorescence of the ocular fundus exhibits retinal pigment epithelium lipofuscin characteristics. Invest Ophthalmol Vis Sci 1995;36:718–729. [PubMed: 7890502]

10. Delori FC, Fleckner MR, Goger DG, Weiter JJ, Dorey CK. Autofluorescence distribution associated with drusen in age-related macular degeneration. Invest Ophthalmol Vis Sci 2000;41:496–504. [PubMed: 10670481]

11. Marmorstein AD, Marmorstein LY, Sakaguchi H, Hollyfield JG. Spectral profiling of autofluorescence associated with lipofuscin, Bruch's membrane, and sub-RPE deposits in normal and AMD eyes. Invest Ophthalmol Vis Sci 2002;43:2435–2441. [PubMed: 12091448]

12. Spaide RF. Fundus autofluorescence and age-related macular degeneration. Ophthalmology 2003;110:392–399. [PubMed: 12578786]

13. Lois N, Halfyard AS, Bird AC, Fitzke FW. Quantitative evaluation of fundus autofluorescence imaged "in vivo" in eyes with retinal disease. Br J Ophthalmol 2000;84:741–745. [PubMed: 10873986]

14. Bone RA, Landrum JT, Cains A. Optical density spectra of the macular pigment in vivo and in vitro. Vision Res 1992;84:105–110. [PubMed: 1502795]

15. Handelman GJ, Snodderly DM, Adler AJ, Russett MD, Dratz EA. Measurement of carotenoids in human and monkey retinas. Methods Enzymol 1992;213:220–230. [PubMed: 1435304]

16. Gellerman W, Bernstein PS. Noninvasive detection of macular pigments in the human eye. J Biomed Opt 2004;9:75–85. [PubMed: 14715058]

17. Bindewald A, Jorzik JJ, Loesch A, Schutt F, Holz FG. Visualization of retinal pigment epithelial cells in vivo using digital high-resolution confocal scanning laser ophthalmoscopy. Am J Ophthalmol 2004;137:556–558. [PubMed: 15013882]

18. Trieschmann M, Spital G, Lommatzsch A, et al. Macular pigment: quantitative analysis of autofluorescence images. Graefes Arch Clin Exp Ophthalmol 2003;241:1006–1012. [PubMed: 14618343]

19. Delori FC, Goger DG, Dorey CK. Age-related accumulation and spatial distribution of lipofuscin in RPE of normal subjects. Invest Ophthalmol Vis Sci 2001;42:1855–1866. [PubMed: 11431454]

20. von Ruckmann A, Fitzke FW, Bird AC. Fundus autofluorescence in age-related macular disease imaged with a laser scanning ophthalmoscope. Invest Ophthalmol Vis Sci 1997;38:478–486. [PubMed: 9040481]

21. Bressler SB, Bressler NM, Seddon JM, Gragoudas ES, Jacobson LP. Interobserver and intraobserver reliability in the clinical classification of drusen. Retina 1988;2:102–108. [PubMed: 3420310]

22. Bird AC, Bressler NM, Bressler SB, et al. An international classification and grading system for age-related maculopathy and age-related macular degeneration. The International ARM Epidemiological Study Group. Surv Ophthalmol 1995;39:367–374. [PubMed: 7604360]

23. Klein R, Davis MD, Magli YL, Segal P, Klein BE, Hubbard L. The Wisconsin age-related maculopathy grading system. Ophthalmology 1991;98:1128–1134. [PubMed: 1843453]

24. Age-Related Eye Disease Study Research G. A randomized, placebo-controlled, clinical trial of high-dose supplementation with vitamins C and E, beta carotene, and zinc for age-related macular degeneration and vision loss: AREDS report no. 8. Arch Ophthalmol 2001;119:1417–1436. [PubMed: 11594942]

25. Bressler NM, Bressler SB, Fine SL. Age-related macular degeneration. Surv Ophthalmol 1988;32:375–413. [PubMed: 2457955]

26. Sunness JS, Bressler NM, Tian Y, Alexander J, Applegate CA. Measuring geographic atrophy in advanced age-related macular degeneration. Invest Ophthalmol Vis Sci 1999;40:1761–1769. [PubMed: 10393046]

27. Lois N, Owens SL, Coco R, Hopkins J, Fitzke FW, Bird AC. Fundus autofluorescence in patients with age-related macular degeneration and high risk of visual loss. Am J Ophthalmol 2002;133:341–349. [PubMed: 11860971]

28. Shin DS, Javornik NB, Berger JW. Computer-assisted, interactive fundus image processing for macular drusen quantitation. Ophthalmology 1999;106:1119–1125. [PubMed: 10366080]

29. Sebag M, Peli E, Lahav M. Image analysis of changes in drusen area. Acta Ophthalmol 1991;69:603–610. [PubMed: 1776413]

30. Morgan WH, Cooper RL, Constable IJ, Eikelboom RH. Automated extraction and quantification of macular drusen from fundal photographs. Aust NZ J Ophthalmol 1994;22:7–12.

31. Kirkpatrick JN, Spencer T, Manivannan A, Sharp PF, Forrester JV. Quantitative image analysis of macular drusen from fundus photographs and scanning laser ophthalmoscope images. Eye 1995;9:48–55. [PubMed: 7713250]

32. Peli E, Lahav M. Drusen measurement from fundus photographs using computer image analysis. Ophthalmology 1986;93:1575–1580. [PubMed: 3808617]

33. Goldbaum MH, Katz NP, Nelson MR, Haff LR. The discrimination of similarly colored objects in computer images of the ocular fundus. Invest Ophthalmol Vis Sci 1990;31:617–623. [PubMed: 2186008]

34. Snodderly DM, Auran JD, Delori FC. The macular pigment. II. Spatial distribution in primate retinas. Invest Ophthalmol Vis Sci 1984;25:674–685. [PubMed: 6724837]

35. Davies NP, Morland AB. Color matching in diabetes: optical density of the crystalline lens and macular pigments. Invest Ophthalmol Vis Sci 2002;43:281–289. [PubMed: 11773043]

36. Rushton WAH, Henry GH. Bleaching and regeneration of cone pigments in man. Vision Res 1968;8:617–631. [PubMed: 5729910]

37. Elsner AE, Burns SA, Webb RH. Mapping cone photopigment optical density. J Opt Soc Am 1993;10:52–58.

38. Weiter JJ, Delori FC, Wing GL, Fitch KA. Retinal pigment epithelial lipofuscin and melanin and choroidal melanin in human eyes. Invest Ophthalmol Vis Sci 1986;27:145–152. [PubMed: 3943941]

39. Smith RT, Nagasaki T, Sparrow JR, et al. A method of drusen measurement based on the geometry of fundus reflectance. Biomed Eng 2003;2:10.

40. Smith RT, Nagasaki T, Sparrow JR, Barbazetto I, Koniarek JP, Bickmann LJ. Photographic patterns in macular images: representation by a mathematical model. J Biomed Opt 2004;9:162–172. [PubMed: 14715069]
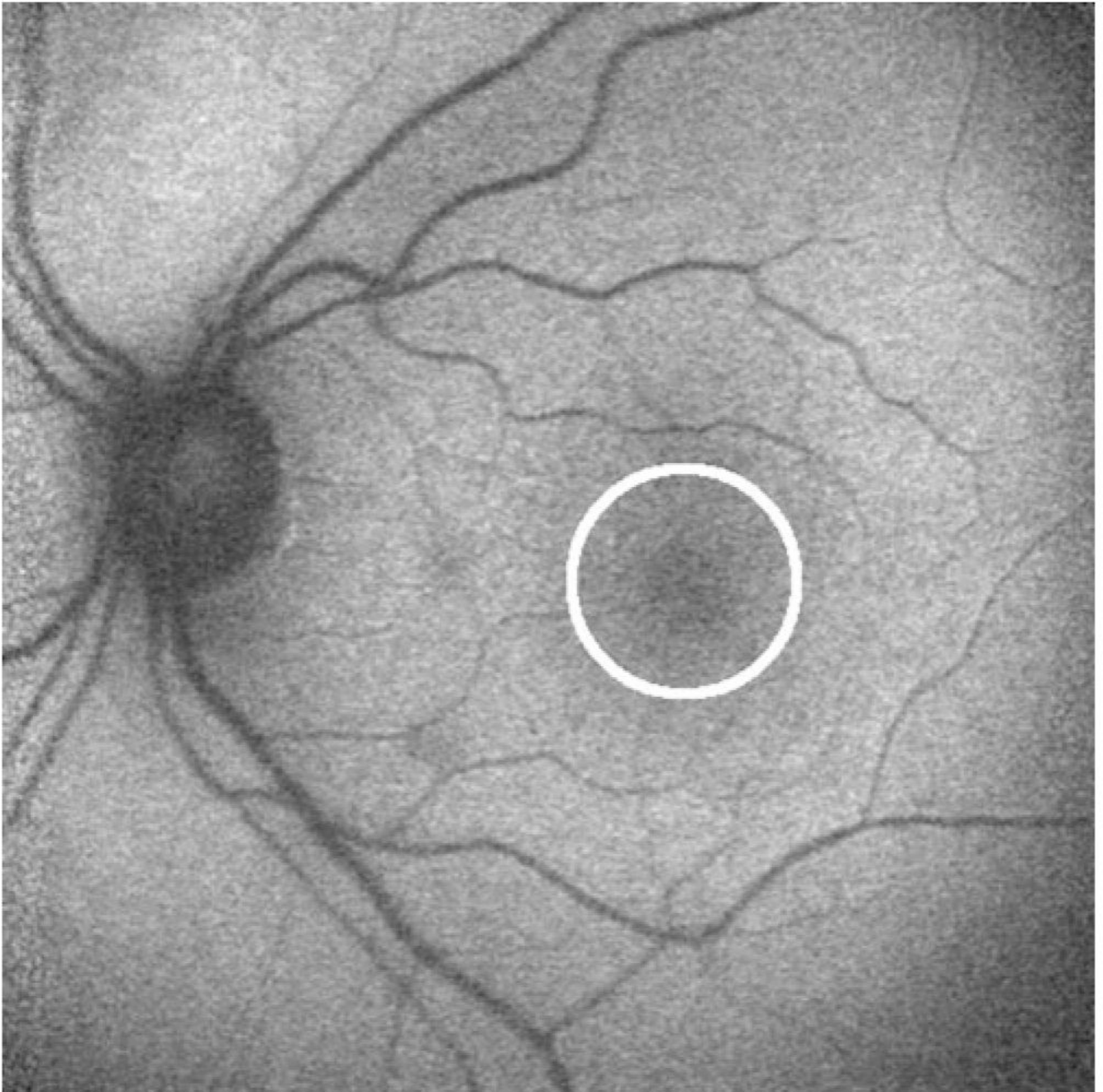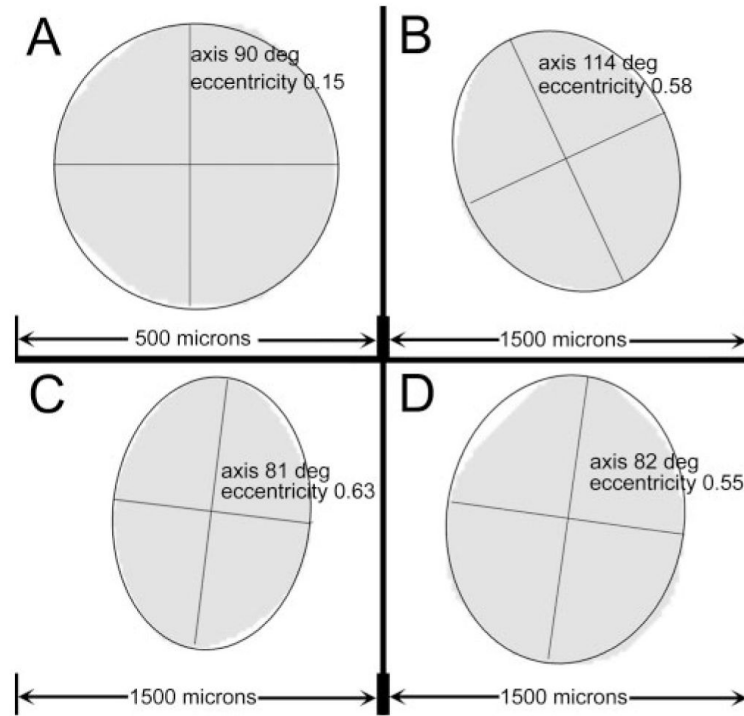
Figure 1.
Typical unfiltered AF image of the left eye of a normal retina of a 50-year-old woman at a resolution of 512 pixels square obtained with the SLO. The *circle* encloses the central foveal region of interest (1500 μm^2 or 100 pixels square). This region is hypofluorescent (*darker*) in the center and becomes progressively hyperfluorescent (*lighter*) away from the center.
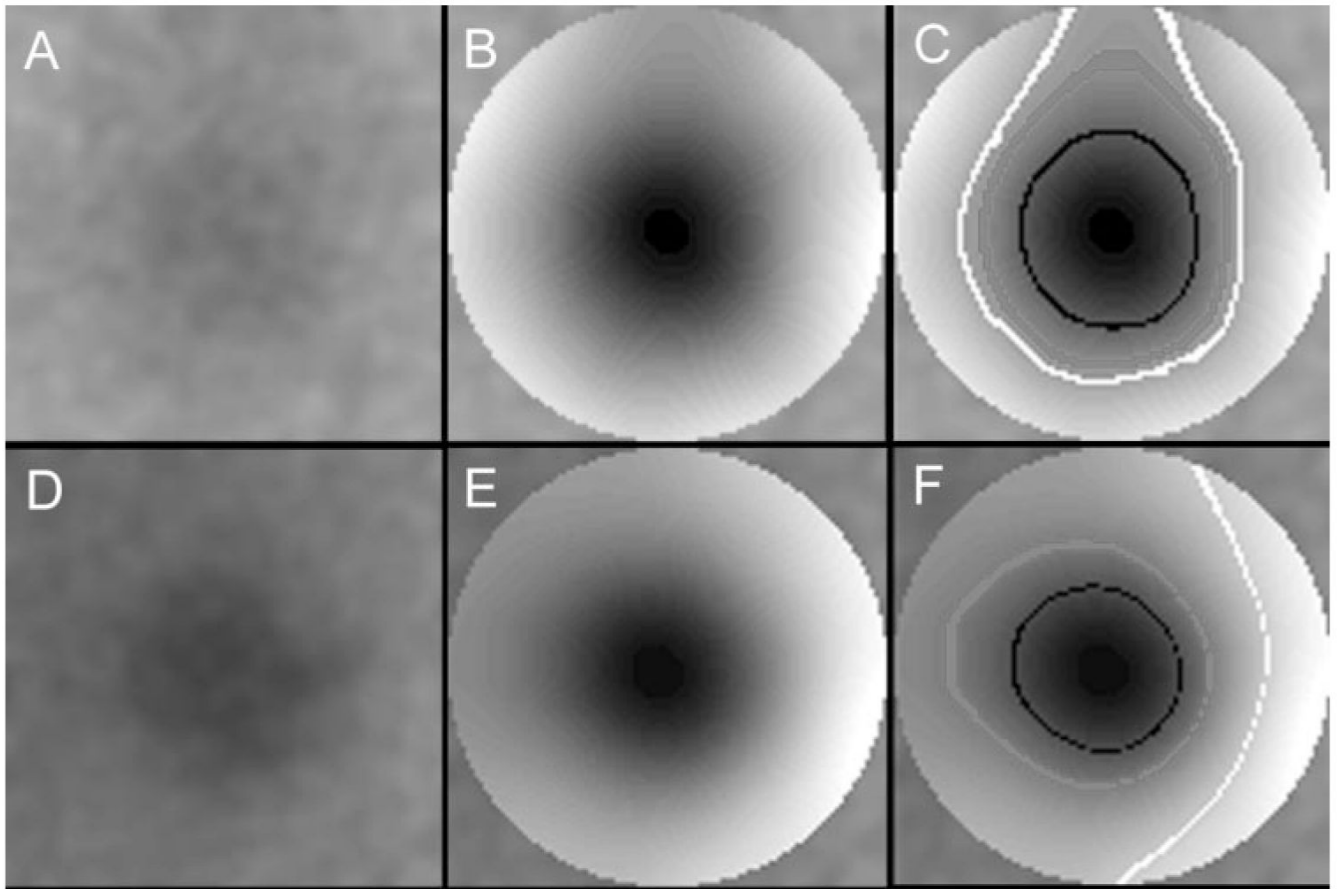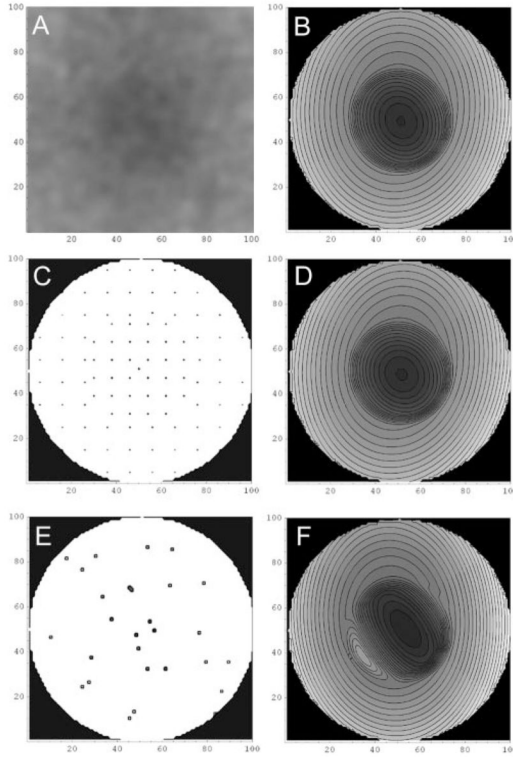
Figure 2.
Filtered foveal images and isobar patterns. (**A**) The foveal region of interest in Figure 1 was filtered on a small scale (Gaussian blur, radius 36 μm) for noise reduction. The central fovea was, on average, more hypofluorescent, but no pattern was apparent. (**B**) The fovea (1500-μm diameter disc) was further filtered (Gaussian blur, radius 180 μm) to establish a very regular shading pattern of concentric elliptical isobars of isofluorescence. Contrast enhancement was applied, to emphasize the geometry of the pattern. The individual isobars were still too fine to be discernible, and so three are highlighted (C) with *black* (original GL = 112, before contrast enhancement), *gray* (original GL = 120), and *white* (original GL = 123). There were 30 isobars in this pattern, yielding an average isobar resolution of 750 μm/30 = 25 μm. The isobars illustrated were even finer, mostly one pixel (15 μm) in width. In this typical pattern, the central isobars were nearly circular, with the more peripheral isobars becoming more vertically elongated until the last were only partial annuli. (**D**) Another normal foveal AF image of the left eye of a 53-year old woman after the small-scale filter was applied. The isobar pattern in (**E**) showed the temporal fovea to be slightly more hyperfluorescent than the other quadrants and the hypofluorescent center appeared somewhat elongated horizontally. These features were dramatically more evident in the individual isobars in (**F**), where isobars are highlighted in *black* (GL = 62), *gray* (GL = 75), and *white* (GL = 97). The ellipses in this less typical pattern became more elongated horizontally and finally became more hyperfluorescent arcs temporally. There were 36 isobars in all in this pattern, yielding an average isobar resolution of 21 μm. The isobars shown are 1 pixel (15 μm) in width, with occasional single pixel discontinuities.
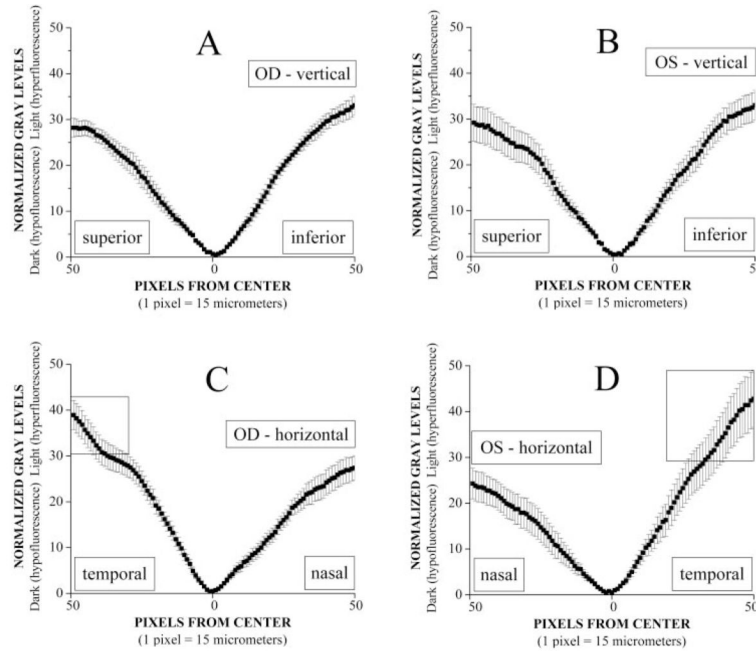
Figure 3.
Ellipses fit to representative AF isobars from patient data. In each panel, the area within a single representative isobar of data is *shaded*. The isobars themselves were thin (as in Figure 2) and shading them facilitates comparison with the calculated bounding ellipse, with major and minor axes in *black*. The axis (the angle made by the major axis with the horizontal) and the eccentricity of each ellipse are displayed. (**A**) The nearly circular fit to a central isobar of diameter 500 μm. (**B**—**D**) Ellipses fit to outer isobars with diameters closer to 1500 μm in three other subjects, with axes clustering around 90° and eccentricities of 0.55 or greater. The isobars are not perfect ellipses, as in (**D**) where the isobar is slightly pear-shaped, but the ellipse fits are clearly close enough that axis and eccentricity are meaningful.

Figure 4.
Modeling and reconstruction of normal AF foveal background. The vertical and horizontal scales on all panels are in pixels. (**A**) Preprocessed foveal AF image of the left eye of a 50-year-old woman. (**B**) Contour graph of the model fit to the complete GL pixel data from the image in (**A**). (The software used for the analysis added the *fine black lines* to delineate individual contours, but they are not part of the model.) The coefficients (*a*, *b*, *c*, *d*, *e*, constant) of the inner and outer quadratics of the model were (0.0297, 0.0087, 0.0367, 0.0278517, -0.00725, 93.6) and (0.00692, -0.0006, 0.0108, -0.0709, 0.0381, 111.7), respectively. (**C**) Uniform grid of pixel data from (**A**)to which the model was fit independently. (**D**) Reconstruction of the foveal AF data from the grid subset of the pixel data in (**C**) by the model. The coefficients of the quadratics fit to the grid data were (0.0318, 0.00778, 0.0353, 0.0762, -0.0303, 93.5) and (0.00676, -0.0014, 0.0111, -0.0553, 0.0331, 111.6), respectively. The model was nearly identical with the model in (**B**). The mean absolute error of the model (**D**) with respect to the image in (**A**) was also nearly as good as that of (**B**; 3.7% compared with 3.6%). (**E**) Random subset of pixel data from (**A**) to which the model was fit independently. (**F**) Reconstruction of the foveal AF data from the random subset of pixel data in (**E**) by the model. The coefficients were (0.0302, 0.0441, 0.0450, -0.160, -0.271, 94.7) and (0.00725, 0.00084, 0.0129, -0.0753, 0.0843, 109.5). The resulting model was quite similar to the model in (**B**) except at the boundary transition inferonasally. The mean absolute error of the model (**F**) with respect to the image in (**A**) is somewhat increased compared with that of (**B**) (5.7% compared to 3.6%).

Figure 5.
Average data (mean ± SE) from normalized horizontal and vertical line scans from right and left foveas of 10 normal subjects. Each scan was normalized by division with respect to the lowest GL near the anatomic center of the fovea. Zero (0) on the *x*-axis represents the location of this most hypofluorescent pixel. The horizontal scale represents single pixel steps (15 *μ*m/pixel). The vertical scale in each graph is the dimensionless GL ratio. (**A**, **B**) The vertical distribution of the GL ratios. The ratios superiorly are not significantly different from those inferiorly. (**C**, **D**) The horizontal distribution of the GL ratios. In the right eyes, the GL ratios for the 9 pixels (135 *μ*m) from the temporal edge (enclosed in a *box*) are significantly higher than the highest GL ratios at the nasal edge of the fovea. In the left eyes, the GL ratios for the 14 pixels (210 *μ*m) from the temporal edge (enclosed in a *box*) are significantly higher than the highest GL ratios nasally.